PIBE: Parallel ion beam etching of sections collected on wafer for ultra large-scale connectomics

Authors: Hongtu Ma[1]†, Yanan Lv[1]†, Minggang Wang[1]†, Zhuangzhuang Zhao[1]†, Lina Zhang[1], Sheng Chang[1], Jing Liu[1], Bohao Chen[1], Xiaohui Dong[1], Yanchao Zhang[1,2], Jinyue Guo[1,2], Haoran Chen[1,2], Hao Zhai[1,2], Linlin Li[1*], Xi Chen[1*], Hua Han[1,2*]

Affiliations:

[1]Key Laboratory of Brain Cognition and Brain-inspired Intelligence Technology, Institute of Automation, Chinese Academy of Sciences, Beijing, China.

[2]School of Future Technology, School of Artificial Intelligence, University of Chinese Academy of Sciences, Beijing, China.

*Corresponding authors. Email: hua.han@ia.ac.cn (Hua Han); xi.chen@ia.ac.cn (Xi Chen); lilinlin@ia.ac.cn (Linlin Li).

†These authors contributed equally to this work.

Abastract: We have developed a parallel ion beam thinning device with low incident ion beam energy, enabling simultaneous 20nm thickness reduction for biological sections which are collected on 4-inch wafer. Together with SEM imaging and volume stitching, it is trustworthy and efficient to achieve three-dimensional electron microscopy imaging of millimeter-scale samples for ultra large scale connectomics.

Introduction

High-resolution electron microscopy (EM) imaging of biological samples is critical in connectomics, where the goal is to map neural circuits in unprecedented detail [1-3]. As this field progresses, efforts to achieve high-resolution imaging of large-scale brain structures, have become a priority for future connectomics research [4]. Achieving this goal requires precise and reliable electron microscopy (EM) imaging of large-scale samples, a task currently challenged by limitations in sample preparation. Traditional EM methods for large specimens rely heavily on ultramicrotomes to produce thousands of ultrathin serial sections [5-8]. However, these methods are limited in terms of achievable axial resolution, as the precision of section thickness is restricted by the mechanical limits of ultramicrotomes, particularly in maintaining stable operation over extended periods [9]. Additionally, the ultrathin sectioning process is highly sensitive to environmental factors such as vibrations and temperature fluctuations, which frequently result in sectioning failures and lower throughput [10]. Consequently, the axial resolution for section-based connectomics typically exceeds 30 nm, hindering the detailed analysis of neuronal connections. In contrast to the limited processing area of Focused Ion Beam Scanning Electron Microscopy (FIB-SEM), Gas Cluster Ion Beam Scanning Electron Microscopy (GCIB-SEM) can achieve high axial resolution while thinning samples over a 7x7 mm^2 area at one operation process [11, 12]. This capability allows for the processing of larger samples, yet for whole mouse brains, the efficiency of thinning several sections simultaneously still falls short of the demands for high-throughput imaging. To address these challenges, we introduce a novel device that employs parallel ion beam thinning technology, adapted

from the semiconductor field. By reducing incident energy of the ion beam, the device can effectively process sections collected on a whole 4-inch wafer simultaneously with a thinning precision of 20 nm. This advancement addresses the axial resolution requirements for ultra large brain samples and significantly enhances the efficiency, scalability and robustness of sample preparation in connectomics, facilitating the study of larger brain regions with higher accuracy and reliability.

In GCIB-SEM, the beam diameter is approximately 250 μm, which necessitates the use of an electrostatic scanning plate to enable rapid deflection of the ion beam across the sample surface [12]. This limitation constrains the effective processing area to less than 10 mm. Moreover, to minimize milling artifacts, the ion beam is typically incident at an angle of 30 degrees, which can lead to uneven thinning across larger samples. This non-uniformity needs additional post-processing steps to achieve the flatness of the imaged 3D volume. In contrast, the Ion Beam Etching method generates a parallel ion beam that delivers uniform energy across a much larger area of up to 150 mm. This capability enables consistent thinning of entire 4-inch wafers without the need for repeated adjustments. Furthermore, the IBE method employs a shallower incident angle of 5 degrees, significantly mitigating the impact of differential sputtering efficiency associated with varying atomic numbers in the sample. This design feature contributes to a more uniform thinning process, enhancing the overall quality and consistency of sample preparation in connectomics research.

Our IBE prototype system consists of control system, vacuum system, RF power supply, ion source, neutralizer, and thinning chamber (Supplementary Fig. 1a, 1b). After being emitted from the ion source, the parallel ion beam enters the thinning chamber to thin the section. The molecular pump provides a vacuum environment of less than 10^{-2} Pa for the thinning chamber. During the ion beam thinning process, to prevent the accumulation of positive charge (such as Ar+ ions) on the sample surface, which could affect the uniformity of the thinning, an equal amount of electrons is released through the neutralizer to neutralize the surface charge in time, thereby ensuring the stability of the thinning process and prevents charging artifacts during SEM image acquisition [13]. The sample stage can be rotated to adjust the thinning angle of the ion beam. The control system is responsible for coordinating the operation of each module, ensuring the stable operation of the system (Supplementary Fig. 2).

Unlike plasma guns such as FIB and GCIB (beam diameters less than 250 μm), IBE can produce parallel ion beams with a diameter of 150mm, due to the unique triple-grid regulation mechanism of its ion source (Fig. 1a, 1b, 1c, Supplementary Fig. 3a). Among them, the coordination between the acceleration grid and the ground grid is primarily used for shaping the ion beam, ensuring its collimation without changing its energy. The ion beams energy is determined by the voltage (80V) applied to the screen grid (Supplementary Fig. 3b). The low ion beam energy is the key to forming a large-area parallel ion beam (see Methods for working principle of triple-gate structure). This ensures that IBE-SEM can achieve a large-area thinning of 4 inches.

The workflow of IBE Scanning Electron Microscopy (IBE-SEM) is shown in Fig. 1d. First, sections of the biological sample resin block are sliced using an ultramicrotome, and the numbered sections are collected onto silicon (Si) pieces. Next, all Si pieces are fixed onto a Si wafer using conductive tape and placed into the SEM for imaging of all the sections in sequence. After imaging, the Si wafer is placed into the IBE thinning chamber for thinning, completing an IBE-SEM cycle. After several IBE-SEM cycles, we will obtain image stacks of all sections. Finally, the image stacks are aligned according to the section numbers to form a three-dimensional volume of the biological

sample.

Results

To evaluate the performance of IBE-SEM for high-resolution volumetric imaging, we prepared sections of mouse prefrontal cortex samples embedded in Pon812 resin (see Methods for samples preparation, Supplementary Fig. 4a). A total of 1010 sections with 100 nm thickness, were obtained and collected on three Si pieces (Supplementary Fig. 4b). These Si pieces were then attached to a Si wafer using conductive tape to ensure good electrical conductivity. The sections were performed with five IBE-SEM cycles (aBSD detection is used for imaging) , after which all 1010 sections were completely milled (4 × 4 × 20 nm voxels). One of the key advantages of IBE-SEM is its ability to achieve a large-area thinning of 4 inches, which improves thinning efficiency and ensures consistent thinning thickness between sections. We used the alignment algorithm (see Methods for serial sections alignment) to reconstruct an 83 μm × 83 μm × 101 μm volume (Fig. 2b). We show SEM images of two consecutive sections at five different refinement depths in the sub-volume, in which neural structures such as postsynaptic density and vesicles are clearly visible. Additionally, the neural structures within and between sections also show good continuity in the SEM images. (Fig. 2a).

To objectively evaluate the axial continuity of IBE-SEM images, we selected ATUM-SEM (Kasthuri, 3 nm × 3 nm × 30 nm)[14] as comparison datasets, both derived from mouse cortex. Qualitatively, compared to ATUM-SEM volumes, the neuronal membrane structures in our IBE-SEM volumes exhibit better continuity and are more easily identifiable across all three views (Supplementary Fig. 5a). In x-z and y-z views, synaptic vesicles are distinguishable in our volumes, however blurred in other volumes (Fig. 2c, Supplementary Fig. 5a). In addition, we quantitatively analyze the image quality using the chunked pearson correlation coefficient (CPC) [15] and structural similarity index measure (SSIM) [16] metrics (Supplementary Note 2). The IBE-SEM dataset improves by 48.2% on CPC and 76.3% on SSIM compared to ATUM-SEM (Supplementary Figure 5b). This indicates that the IBE-SEM dataset has better structural continuity between sections.

We densely reconstructed a sub-volume of 83 μm × 83 μm × 26.4 μm using a watershed-agglomeration method (Fig. 2d, Supplementary Fig. 6). Fig. 2d shows spiny dendrites along with synapsing axons spanning an IBE-SEM volume of 261 sections. Fig. 2e shows views through a single spiny synapse. As is known to all, one of the biggest bottlenecks in automatic dense reconstruction algorithm is the segmentation of thinnest structures, such as axons (diameter of 1 μm) and dendrite spines (diameter of 0.5-2 μm) [14]. To further illustrate the superiority of fine structure segmentation IBE-SEM, we compare the performance of dendrite reconstruction between IBE-SEM and ATUM-SEM. In our IBE-SEM volumes, 76.3% of the spines on the dendrites can be accurately segmented without proofreading. In contrast, using the same automated segmentation algorithm (see Methods for 3D reconstruction of the neurons in the cytoplasm), only 31.2% of the spines are attached in the ATUM-SEM volumes (Supplementary Fig. 7a). This indicates that the IBE-SEM volumes have good performance for fine structure segmentation. Furthermore, the fragmentation of the spine neck is more severe in the ATUM-SEM volume (Supplementary Fig. 7b), which greatly affect the subsequent proofreading.

To further illustrate the advantages of IBE-SEM in large-volume imaging, we prepared sections of mouse prefrontal cortex samples embedded in Pon812 resin (see Methods for samples preparation). A total of 150 sections, each 100 nm thick (Supplementary Fig. 8a). The sections were

performed to five IBE-SEM cycles (aBSD detection is used for imaging) , during which all 150 sections were completely milled (10 × 10 × 20 nm voxels). we used the alignment algorithm (see Methods for serial sections alignment) to reconstruct a 1721μm × 550μm × 15μm volumes (Supplementary Fig. 8c). The experimental results show that IBE-SEM is capable of imaging large volumes at the millimeter scale without cutting the sample into smaller volumes. This technique is particularly suitable for processing large nuclear clusters within the entire mouse brain or brain regions, which is a significant advantage over FIB and GCIB techniques. Furthermore, we developed an algorithm for automatically detecting synapses and mitochondria in the millimeter-scale IBE-SEM volume (see Methods for 3D reconstruction of the ultrastructures). The raw images and their detection results clearly show that this imaging technology and alignment algorithm meet the demands for ultrastructure reconstruction, with synaptic and mitochondrial features, particularly the PSD features of synapses, clearly discernible (Supplementary Fig. 9).

To validate the applicability of IBE-SEM for thick section processing, we prepared continuous brain sections with a thickness of 500nm and a size of 3mm×3mm (Supplementary Fig.10a, 10b). The sections were performed to fourteen IBE-SEM cycles, with a Z-axis resolution of 35.7nm (Supplementary Fig.10c). Additionally, we specifically observed the continuity of organelles such as dendritic spines, mitochondria, and the endoplasmic reticulum. Our data shows that IBE-SEM can clearly capture the fine structure of neural networks with good continuity.

Discussion

In summary, we developed an IBE-SEM workflow utilizing parallel ion beam thinning technology, enabling robust and efficient acquisition of three-dimensional electron microscopy images of large-scale samples with a z-direction resolution of 20 nm. Based on feasibility, efficiency, cost and other factors, the method based on etching thinning and scanning electron microscopy imaging may become a feasible technical solution for the finer structure reconstruction of ultra-large-scale brain connectomes.

Methods

Animals

All animal experiments were conducted in accordance with the regulations of the animal care agency and the Beijing Municipal Regulations for the management of laboratory animals. The rats used in this experiment were housed in the Experimental Animal Center of Tsinghua University, adhering to the standards for experimental rat care. The facility is graded as specific pathogen-free (SPF) to ensure that the animals are in a controlled environment. The housing conditions included a 12-hour light/dark cycle, a stable temperature of 24±1°C, relative humidity of 35±4%, with water and food available ad libitum.

Samples preparation

All experimental protocols complied with relevant ethical regulations. After the rats were anesthetized with isoflurane inhalation, they underwent cardiac perfusion fixation. First, the blood was quickly flushed with 0.1 M phosphate buffer (PB). Then, a solution of 2% paraformaldehyde (PFA) and 1.25% glutaraldehyde (GA) in 0.1 M PB was quickly perfused. The perfusion of the fixative was then slowed down and continued for no longer than 20 minutes. After the perfusion, the mouse's cerebral cortex was removed. Small sample blocks, approximately 1 mm^3 in size, were trimmed from the mouse cerebral cortex and postfixed in a solution of 4% PFA and 2.5% GA in 0.1 M PB and kept at 4°C overnight. The samples were then washed using deionized water. The postfixation was carried out with 2% OsO_4 (Ted Pella, 18451), prepared in 0.1 M PB, for a duration of 90 minutes at room temperature. Next, the samples were placed in a solution of 2.5% ferrocyanide (Sigma, 234125) in 0.1 M PB and incubated at room temperature for 90 min. Then, after washing three times with deionized water the samples were incubated in a solution of thiocarbohydrazide (TCH, Sigma, 223220) at 40°C for 45 min. After TCH treatment, the samples were thoroughly washed with deionized water and then incubated with 2% OsO_4 for 90 min. The samples were then transferred to a new centrifuge tube for washing. After that, they were incubated with 1% uranyl acetate (SPI-chem, 02624-AB) at 4°C overnight. The samples were incubated with lead aspartate solution (0.033 g lead nitrate (Sigma, 228621) dissolved in 5 mL 0.03 M aspartic acid (Sigma, 11189, pH 5.0)) at 50°C for 90 minutes. Then, the samples were dehydrated through a graded ethanol (50%, 70%, 80%, 90%, 100%, 10 min each) and pure acetone on a horizontal shaker. Subsequently, the samples were infiltrated with Epon-812 resin (SPI, Epon-812), also on a horizontal shaker. The samples were immersed in epoxy/acetone solutions with increasing epoxy concentrations: 1:1, 2:1 and 3:1, and each immersion lasted 4-8 hours. Then, pure epoxy resin was infiltrated twice under negative pressure, each immersion lasted 4-8 hours. The last step was polymerization. The samples were placed in an embedding plate and processed at 60°C for 24 hours.

Sectioning, thinning and imaging

IBE-SEM is composed of our self-developed IBE prototype machine and the Zeiss Gemini 0300 scanning electron microscope. Since the IBE can thin thousands of sections in just a few minutes, the imaging speed of IBE-SEM is mainly limited by the SEM speed. Parallel imaging with multiple SEMs will greatly enhance the speed of IBE-SEM. To retain the parallel processing capability of IBE-SEM, we did not integrate the IBE with the SEM. The core component of the IBE, the ion source, is purchased from Beijing SHL Company.

Sectioning: First, the Si wafer is cut into 2×3 mm Si pieces using a dicing saw and cleaned and hydrophilized using a plasma cleaner. Then, an appropriate amount of water is added to the diamond knife boat (Supplementary Figure 4a), and a thin layer of a mixture of Pattex glue (Henkel, Düsseldorf, Germany) and xylene (1:500) is applied on the side of the diamond knife that contacts the water, allowing the sections to stick together and form strips, thus preventing the sections from scattering. We use a room temperature diamond knife (35° angle) on an ultramicrotome (LEICA EM UC7) to slice from the mouse frontal cortex embedded in Pon812 (Supplementary Figure 4a). These slices are collected onto multiple 3×2 cm Si pieces. Finally, all the Si pieces are glued to the Si wafer with conductive tape to ensure good conductivity.

Mouse cortex (83 μm × 83 μm × 101 μm imaging volume): Mouse cortex was sectioned. A total of 1010 sections (each section with 100 nm thickness) were collected on three 3 × 2 cm Si pieces (Supplementary Fig. 4b). The three Si pieces were then attached to the Si wafer with conductive tape. Five IBE-SEM cycles (Fig. 2d) were then performed to complete the thinning of all sections. The IBE parameters used were as follows: ion beam energy of 80V, ion beam current of 100 mA, acceleration voltage of 400V, etching angle of 85°, neutralizing beam current of 400 mA, neutralizing gas flow rate of 7 sccm, ion beam diameter of 150 mm, and etching rate of 0.0277 nm/s; each IBE-SEM cycle lasted 720 seconds, with an etching depth of 20 nm. The SEM parameters used were: a Gemini 0300 equipped with a field emission gun (Zeiss, Germany) for continuous section SEM imaging, with the following specific parameters: acceleration voltage of 5 kV, aBSD detection, pixel size of 4 nm, and dwell time of 300 ns.

Mouse cortex (1721 μm × 550 μm × 15 μm imaging volume): Mouse cortex was sectioned. A total of 150 sections (each slice with 100 nm thickness and dimensions of 3×3 mm) were collected on five 3 × 2 cm Si pieces (Supplementary Fig. 8a). The five Si pieces were then attached to the Si wafer with conductive tape. Five IBE-SEM cycles (Fig. 2d) were then performed to complete the thinning of all sections. The IBE parameters used were as follows: ion beam energy of 80V, ion beam current of 100 mA, acceleration voltage of 400V, etching angle of 85°, neutralizing beam current of 400 mA, neutralizing gas flow rate of 7 sccm, ion beam diameter of 150 mm, etching rate of 0.0277 nm/s, with an etching time of 720 seconds per IBE-SEM cycle and an etching depth of 20 nm. The SEM parameters used were: continuous section SEM imaging with a Gemini 0300 equipped with a field emission gun (Zeiss, Germany). The SEM parameters were: acceleration voltage of 5 kV, aBSD detection, pixel size of 10 nm, and dwell time of 300 ns.

500 nm thick mouse brain sections: 500 nm thick sections were sectioned from the mouse brain. The sections were collected onto the Si wafer, and fourteen IBE-SEM cycles were performed to completely thin all the sections. The IBE parameters used were as follows: ion beam energy of 80V, ion beam current of 100 mA, acceleration voltage of 400V, etching angle of 85°, neutralizing beam current of 400 mA, neutralizing gas flow rate of 7 sccm, ion beam diameter of 150 mm, etching rate of 0.0277 nm/s, with an etching time of 1285 seconds per IBE-SEM cycle and an etching depth of 35.7nm. The SEM parameters used were: continuous section SEM imaging with a Gemini 0300 equipped with a field emission gun (Zeiss, Germany). The SEM parameters were: acceleration voltage of 5 kV, aBSD detection, pixel size of 10 nm, and dwell time of 300 ns.

Serial sections alignment

The imaging process for serial sections is shown in Supplementary Fig. 11. Since the section area is much larger than the field of view (FOV) of the electron microscope, we imaged the sections as partially overlapping 2D tiles (the overlap is about 10-15%) by moving the microscope stage. Then, the tiles of each section were stitched into a large image. In the practical stitching process, we first extracted the corresponding point pairs from the overlapping region between adjacent tiles and used these point pairs to calculate the translation between adjacent tiles. Then, we utilized a least squares method to globally optimize the position of each tile. Finally, we obtained the entire seamless image for each section.

We adopted a 'divide-and-conquer' strategy to align serial section images. Assuming each section was thinned 4 times, 5 consecutive images were obtained from each section. To align long serial sections, we divided every 6 sections (i.e., 30 images) into a stack, which became the main unit for subsequent alignment. We then selected the first image of each stack to form a reference sequence. Affine transformations were applied to correct linear deformations in the reference sequence. This ensured that each pair of adjacent reference images corresponded to the beginning and end of each stack, and the reference images in each stack remained constant throughout the alignment process.

During the coarse alignment process, images of the stacks were downsampled by 32X. We first performed pairwise alignment between every two adjacent images, extracted the corresponding points and applied affine transformations to estimate their deformations, and then gradually extended to the entire stack. In pairwise alignment, CUDA-SIFT [17] was used to extract feature points of images, and the RANSAC [18] algorithm was used to filter corresponding point pairs. After pairwise alignment, we propagated the deformations across the entire stack. to complete the coarse alignment. In fine alignment of each stack, we used an unsupervised optical flow network [19] to measure feature similarity between adjacent images. The optical flow network was then employed to estimate and compensate for cumulative registration error, thereby allowing for the reconstruction of the structure of biological tissues. Based on the above steps, we implemented the reconstruction of 3D volume from serial sections.

3D reconstruction of the neurons in the cytoplasm

We applied a watershed-agglomeration method to obtain the dense reconstructions from IBE-SEM volumes. To construct the ground-truth dataset more efficiently, we annotated the neurons based on an imperfect segmentation instead of starting from scratch. Specifically, we first generated an initial segmentation of a 2000 × 2000 × 30 voxels IBE-SEM volume using a network trained on other ATUM-SEM volumes, and then annotators checked through all the neurons and proofread the segmentation errors.

We chose another two IBE-SEM volumes of different regions and adopted a semi-supervised strategy to learn the affinity maps from labeled and unlabeled raw data. We first used the labeled training data and trained a 3D Residual U-Net in a supervised way, then the network was fine-tuned by performing the semi-supervised method. The SGD optimizer with a learning rate of 0.0001 was used. Supervised training and semi-supervised training each contained 100,000 iterations, respectively. All networks were implemented in PyTorch and conducted on one NVIDIA V100 GPU.

Using the trained network, we ran the inference on a large volume with a size of 83 μm × 83 μm × 26.4 μm and obtained an affinity map of the same size. The 2D distance-transform-

watershed algorithm was applied to each section to generate 2D superpixels. Then superpixels were agglomerated based on the multicut pipeline. The edge probability was computed by the mean affinity value accumulated on each edge. The hyper-parameter Beta was set as 0.5. We used GAEC to solve the multicut problem. For comparison, we executed experiments using the same training strategy on the Kasthuri dataset [14]. Specifically, the labeled data were extracted from the labeled subset AC4, while the unlabeled data were sourced from AC3. The size of the training data was consistent with that of IBE-SEM.

3D reconstruction of the ultrastructures

To avoid extensive manual annotation, we leveraged existing labeled data to reconstruct synapses and mitochondria using deep learning techniques in electron microscopy imagery. Specifically, we employed pre-existing mammalian annotation data to generate a pretrained model. Synapses encompassed volumes from the prefrontal cortex of rats [20] and the auditory cortex of mice [21], while mitochondria encompassed volumes from the prefrontal cortex of rats [20]. All images were obtained via ATUM-SEM imaging at a resolution of 50nm × 6nm × 6nm. We set the batch size to 2 and the patch size to 16 × 320 × 320, feeding them into a six-level nnUNet[22]. The model was optimized using SGD with a momentum of 0.9 for better generalization [23], and trained using a "poly" learning rate strategy [24] with an initial learning rate of 0.1.

Following the training of the segmentation model, we partitioned the inference volume data, sized 757 × 10000 × 10000, into blocks of 50 × 1024 × 1024. Considering the receptive field and object scale, we set the overlap between each block and its adjacent blocks to 2 × 126 × 126. The data were interpolated bilinearly before being input into the model. After getting the probability map, the predictions were restored to the original resolution and binaryized using a softmax function. Instances of synapses and mitochondria were differentiated using connected components within sub-blocks and merged within overlapping regions to the global volume. The model was implemented using PyTorch and executed on an NVIDIA Tesla V100 GPU.

Working principle of triple-gate structure

Unlike plasma guns such as FIB and GCIB, IBE is capable of generating a large-area uniform ion beam, thanks to the unique triple-grid regulation mechanism of its ion source (Fig. 1a, 1c, 1d, Supplementary Fig. 2a). First, in the plasma chamber of the IBE ion source, high-energy electrons are excited by radio frequency (RF) and collide with argon gas molecules, causing ionization of the argon molecules and generating a large number of free electrons and Ar+ ions, thereby forming plasma. Then, after applying a voltage (80V) on the screen grid, Ar+ ions are extracted from the plasma chamber, while electrons are shielded within the plasma chamber. This effectively reduces the interference of low-energy electrons on the ion beam, ensuring the purity of the ion beam. Next, the ion beam is shaped by passing through the acceleration grid (-400V), which improves the uniformity and collimation of the ion beam. The voltage of the acceleration grid needs to be precisely adjusted based on the screen grid voltage. If the acceleration grid voltage is too low, the ion beam will not be effectively collimated. Conversely, if the voltage is too high, the ion beam will be completely absorbed by the acceleration grid, preventing the ion beam from being emitted properly. Finally, the ion beam undergoes deceleration through the grounded grid, forming a low-energy ion beam. The coordination of the acceleration grid and grounded grid is mainly used for shaping the ion beam, without changing its energy, which is determined by the voltage applied to

the screen grid (Supplementary Fig. 2b). Ultimately, the Ar+ ions are extracted and shaped by the triple-grid system, forming a parallel ion beam with a diameter of 150mm.

Indicators of CPC and SSIM

In order to evaluate the axial continuity of the reconstruction results, this work introduced two evaluation indicators: the chunked pearson correlation coefficient (CPC) [15] and structural similarity index measure (SSIM) [16]. CPC is used to evaluate the correlation between two images in the local (block) area, while SSIM is used to measure the structural similarity of the two images. The aligned images in the datasets are evenly divided into image chunks without overlapping, as performed in [15]. The image chunks at the same horizontal position in adjacent sections are defined as matching pairs. The resolution of the input image was downsampled to approximately $30 \times 30\, nm^2/pixel$, and each image chunk has a size of 64 × 64, which corresponds to a region of approximately $2 \times 2\ \mu m^2$ at this resolution. Following the chunk division process, these criteria were computed for each matching pair independently. Unless otherwise specified, no additional pre-processing (e.g., histogram normalization) is applied to the matching pairs.

The CPC and SSIM values (Supplementary Fig. 5) of the IBE-SEM dataset are mainly concentrated in the high-value range (CPC > 0.64, SSIM > 0.57), indicating good alignment quality between adjacent sections. The CPC values of the ATUM-SEM dataset are concentrated around 0.468, which is significantly lower than our dataset. The distribution of SSIM criteria also exhibits a similar trend. These results indicate that the IBE-SEM dataset has better inter-section structural alignment quality compared to the contrast datasets. Noticeably, the criterion distribution of the etching dataset exhibits a bimodal trend. This is primarily due to the abrupt contrast changes caused by the residual thickness of the sample during the imaging process, as shown in Supplementary Fig. 8b. We conducted detailed manual inspections on image data with significant inter-section contrast differences. The results indicate that the low criterion values in these matching-pairs are solely caused by inter-section contrast differences, but not genuine misalignments. This conclusion demonstrates that the etching dataset possesses good alignment quality, which can provide a reliable data foundation for subsequent reconstruction and analysis tasks.

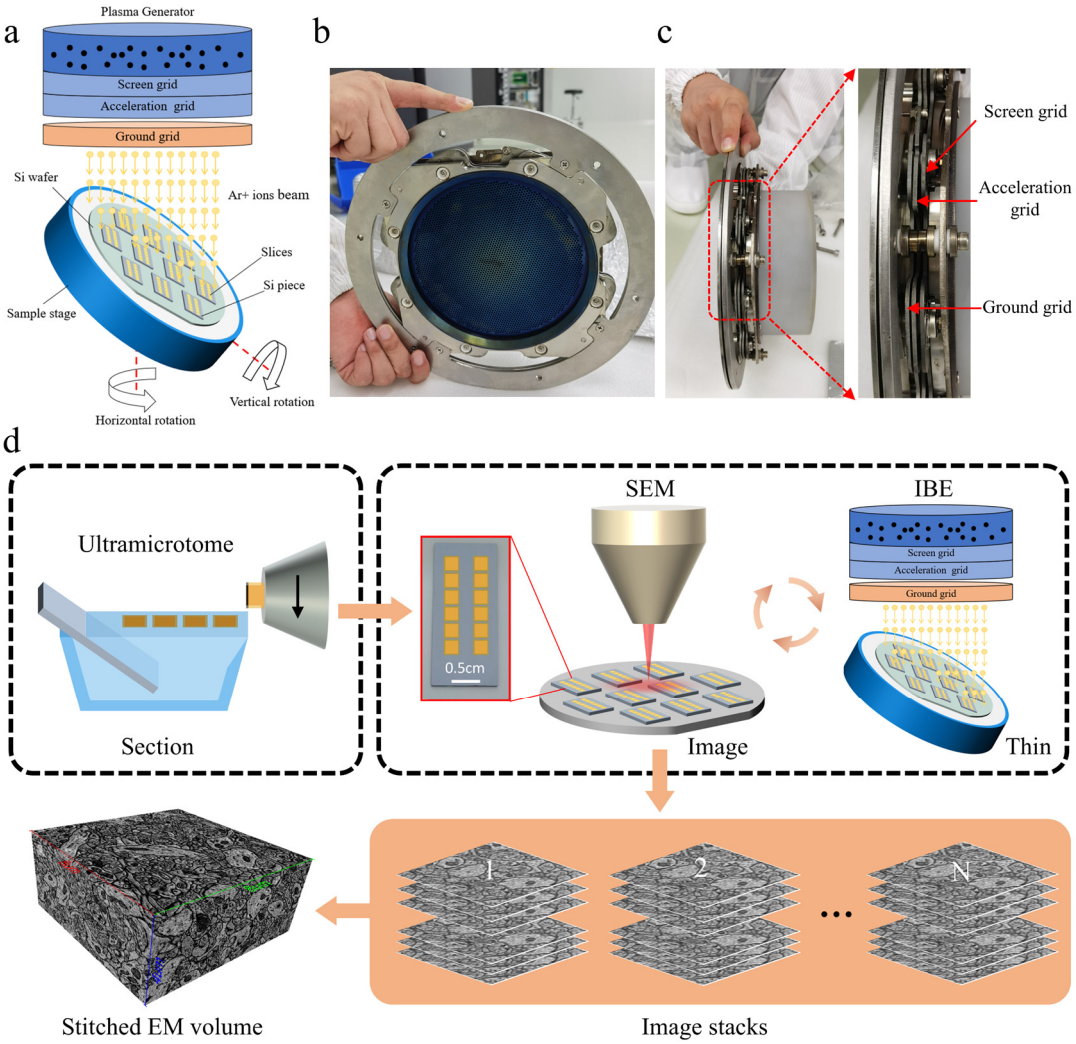

Fig. 1 | IBE-SEM overview. a, Schematic diagram of IBE-SEM working principle. After the plasma is generated, it is extracted and shaped by the three-grid structure to form a large-area parallel ion beam for thinning sections. **b**, Front view of the ion source grid assembly. **c**, Side view of the ion source grid assembly showing the triple-grid structure, which includes the screen grid, acceleration grid, and ground grid. **d**, The workflow of IBE-SEM.

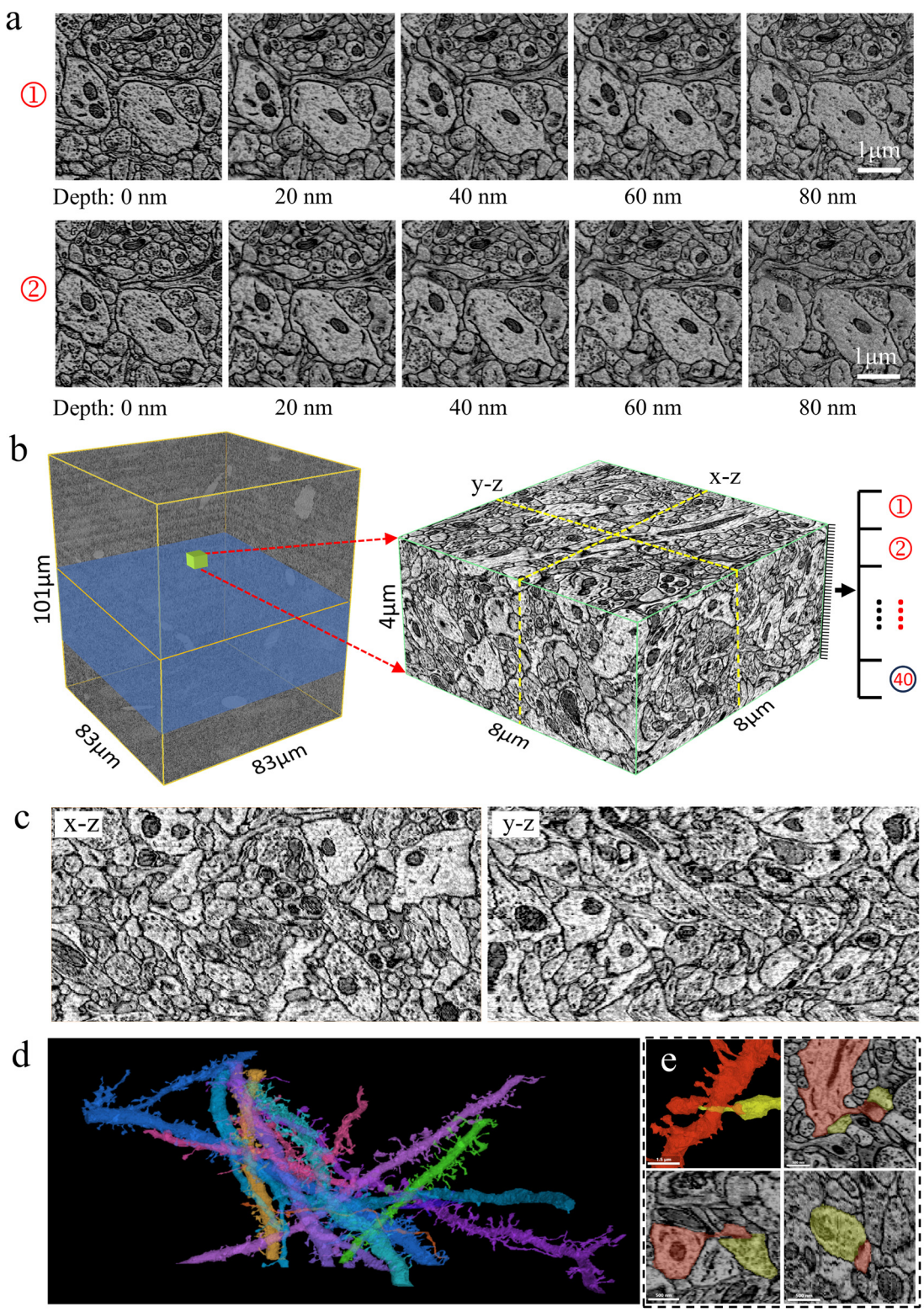

Fig. 2 | Imaging of a cubic 100 um of mouse cortex by the continuous section etching thinning imaging. a, SEM images of two consecutive sections in the sub-volume at five different thinning depths. **b**, A stitched stack is shown as a 3D volume, which includes reconstructed complete volume (83μm × 83μm × 101μm) and clear local volume (8μm × 8μm × 4μm), which consists of 40 sections with 100 nm thickness. **c**, The x-z and y-z views of the yellow dashed line position in the sub-volume. **d**, The x-z view of the reconstructed dendrites without proofreading in the blue region of

the 83μm × 83μm × 101μm (b) volume. Reconstructed volume size 83μm × 83μm × 26.4μm. **e**, Reconstructions of thin structures: dendrite spine (red) and axon bouton (yellow).

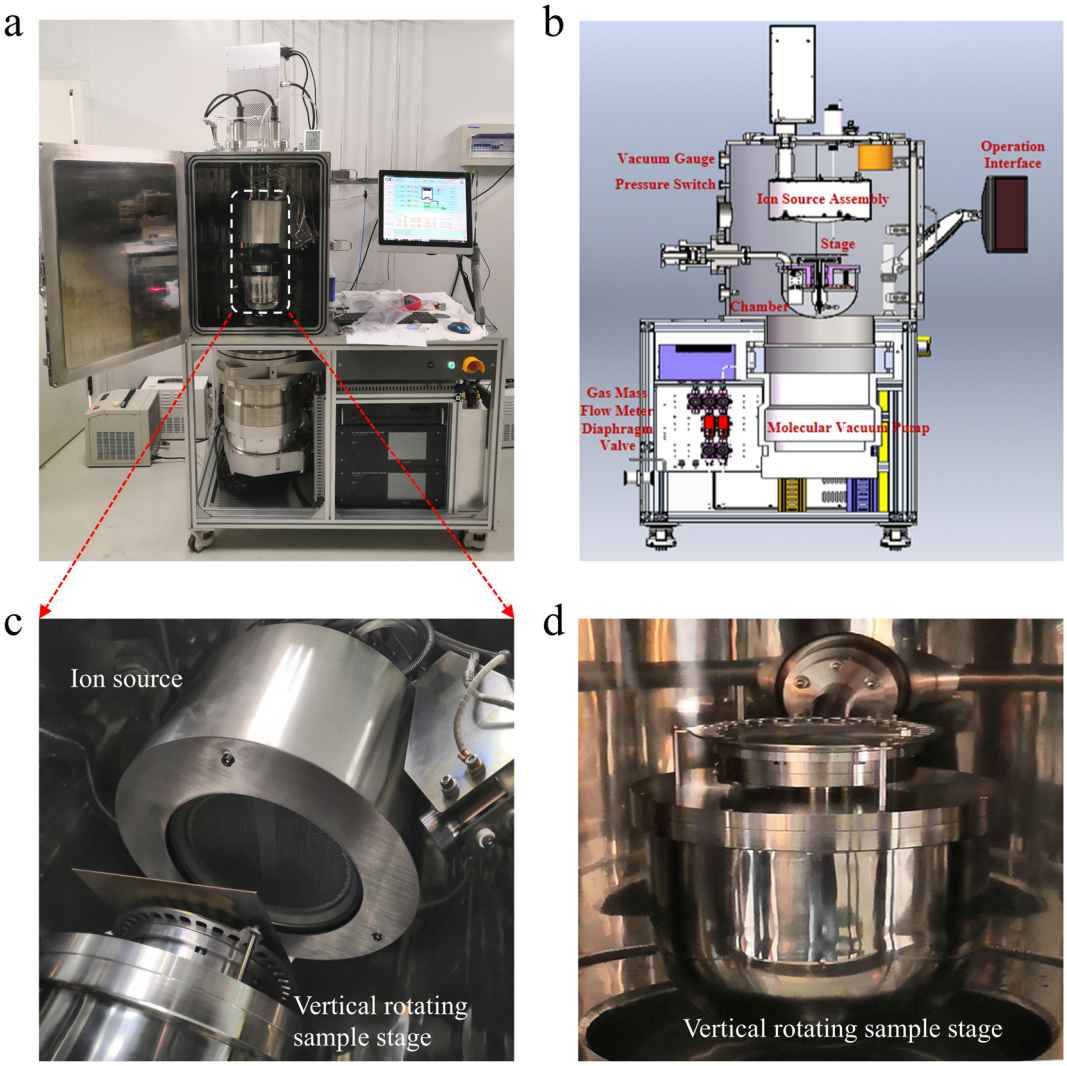

Supplementary Fig. 1. IBE prototype system. a, IBE prototype system consists of a control system, vacuum system, RF power supply, ion source, neutralizer, and thinning chamber. The neutralizer is installed inside the thinning chamber. **b,** IBE system working principle diagram. **c,** Vertical rotating sample stage.

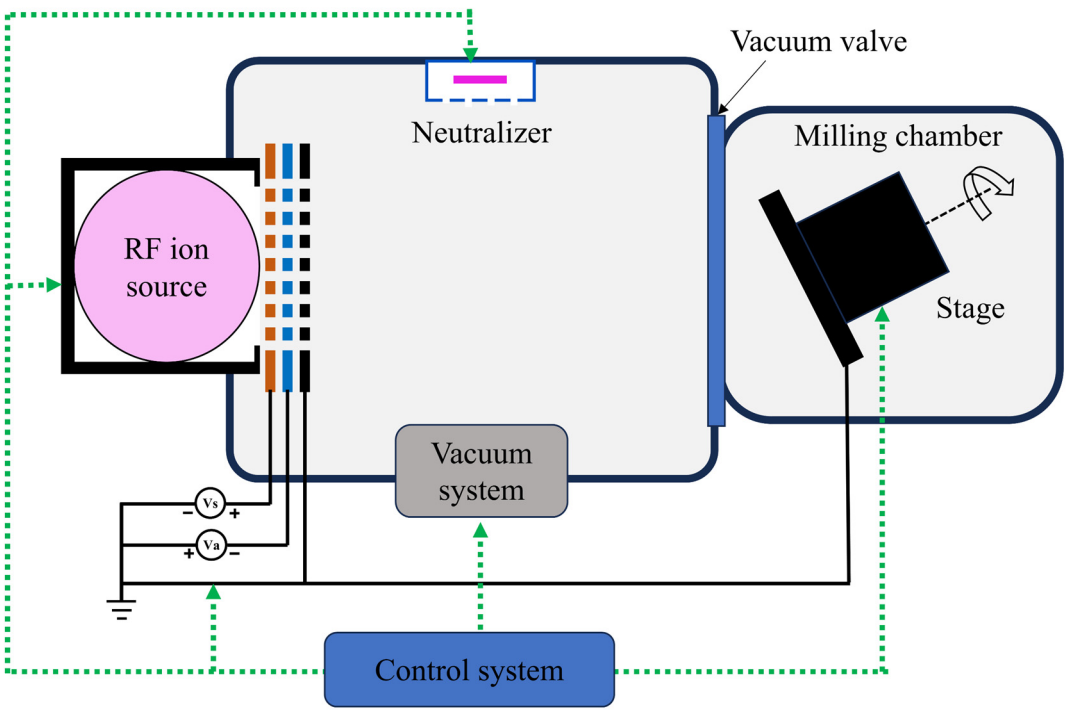

Supplementary Fig. 2. Operational Mechanism of the IBE Prototype. After the parallel ion beam is emitted from the ion source, it enters the thinning chamber for slicing and thinning. The molecular pump provides a vacuum environment of less than 10^{-2} Pa for the thinning chamber. During the ion beam thinning process, to prevent the accumulation of positive charge (such as Ar+ ions) on the sample surface, which could affect the uniformity of the thinning, an equal amount of electrons is released through the neutralizer to neutralize the surface charge in time, ensuring the stability of the thinning process. The sample stage can rotate vertically to adjust the thinning angle of the ion beam. The control system is responsible for coordinating the operation of each module, ensuring the stable operation of the system.

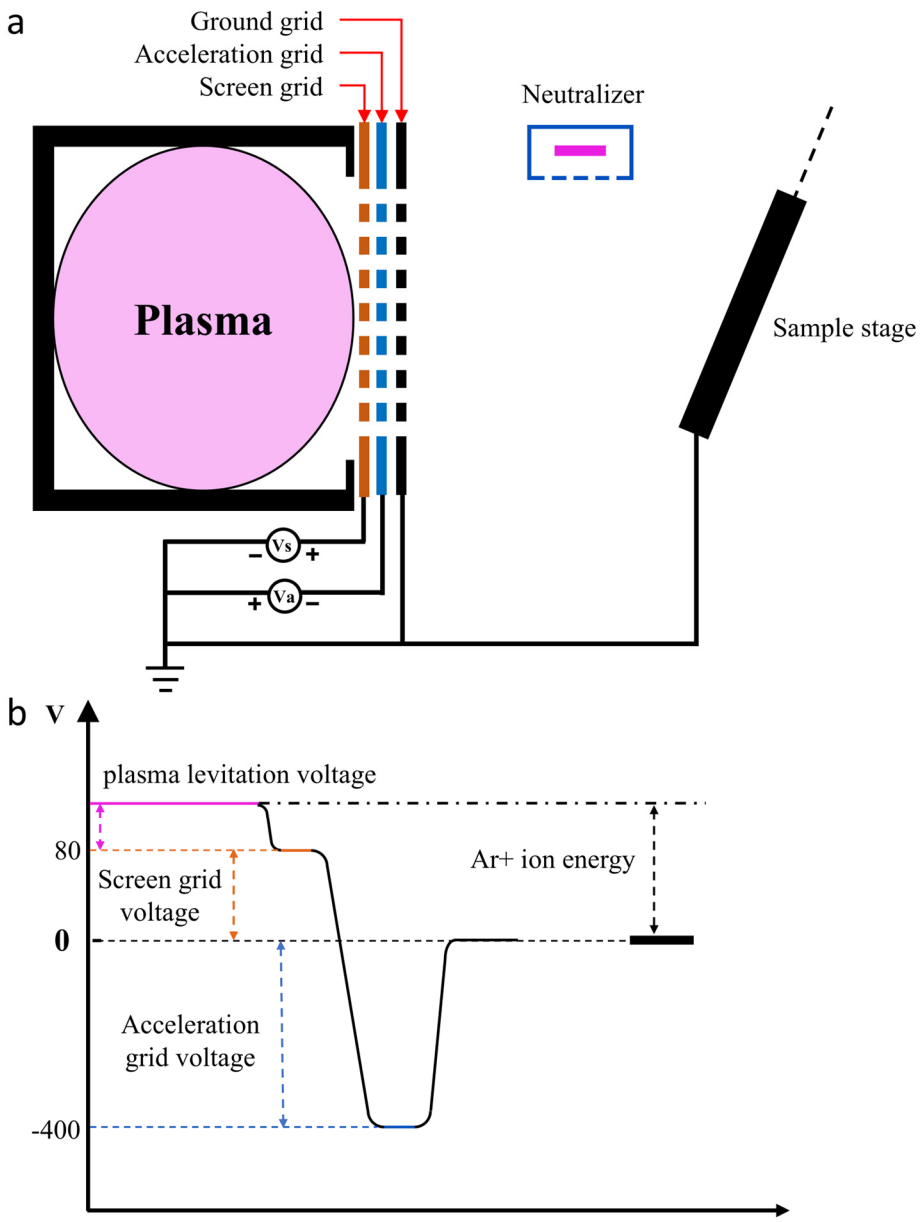

Supplementary Fig. 3. Ion source system. a, The ion source consists of a plasma chamber and a three-grid structure (screen grid, acceleration grid and lower grid). **b,** Energy level diagram of three-grid structure. In the plasma chamber of the IBE ion source, high-energy electrons collide with argon gas molecules through radio frequency (RF) excitation, causing ionization of the argon molecules and generating a large number of free electrons and Ar+ ions, thereby forming a plasma. Under the negative voltage (80V) applied to the screen grid, the Ar+ ions are extracted from the plasma chamber, while the electrons are shielded within the plasma, reducing interference from low-energy electrons in the ion beam and ensuring the purity of the ion beam. The ion beam is then shaped by an acceleration grid (400V) to achieve high uniformity and collimation. The coordination between the acceleration grid and the ground grid is only used for shaping the ion beam and does not alter its energy.

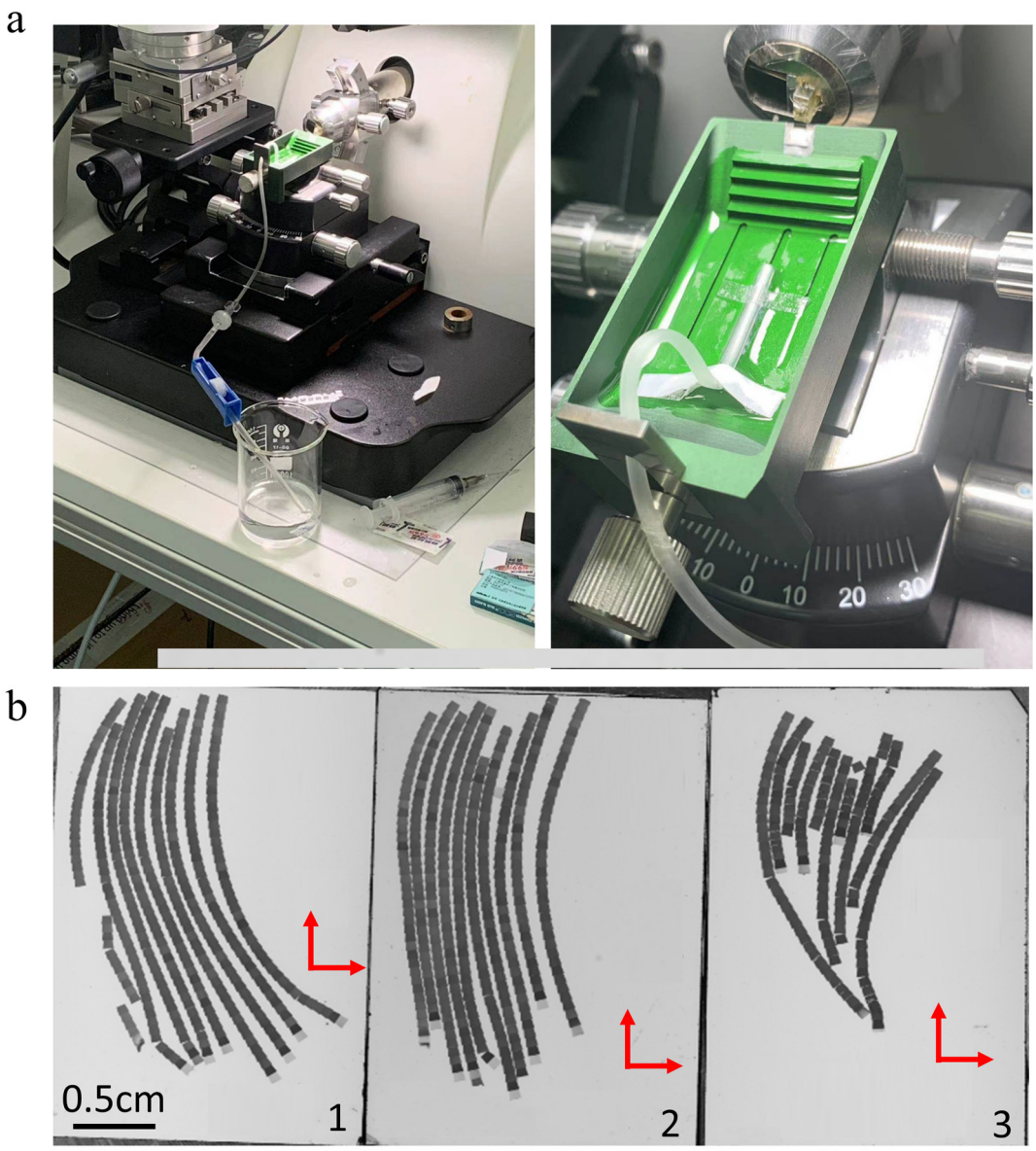

Supplementary Fig. 4. A custom-built device to mount ribbons of serial sections onto a hydrophylized silicon wafer. A. Left, Positioning of the device in the diamond knife boat. Positioning of the plastic conduit and syringe in the diamond knife boat; Right, Close-up showing the position of the wafer close to the edge of the diamond knife. A tissue block mounted on the microtome arm is visible on the left. **B.** The 83 µm × 83 µm × 101 µm volume of mouse cortex is sectioned using an ultramicrotome, resulting in 1010 slices, each 100 nm thick. The sections are collected onto three silicon wafers, each measuring 2 cm × 3 cm.

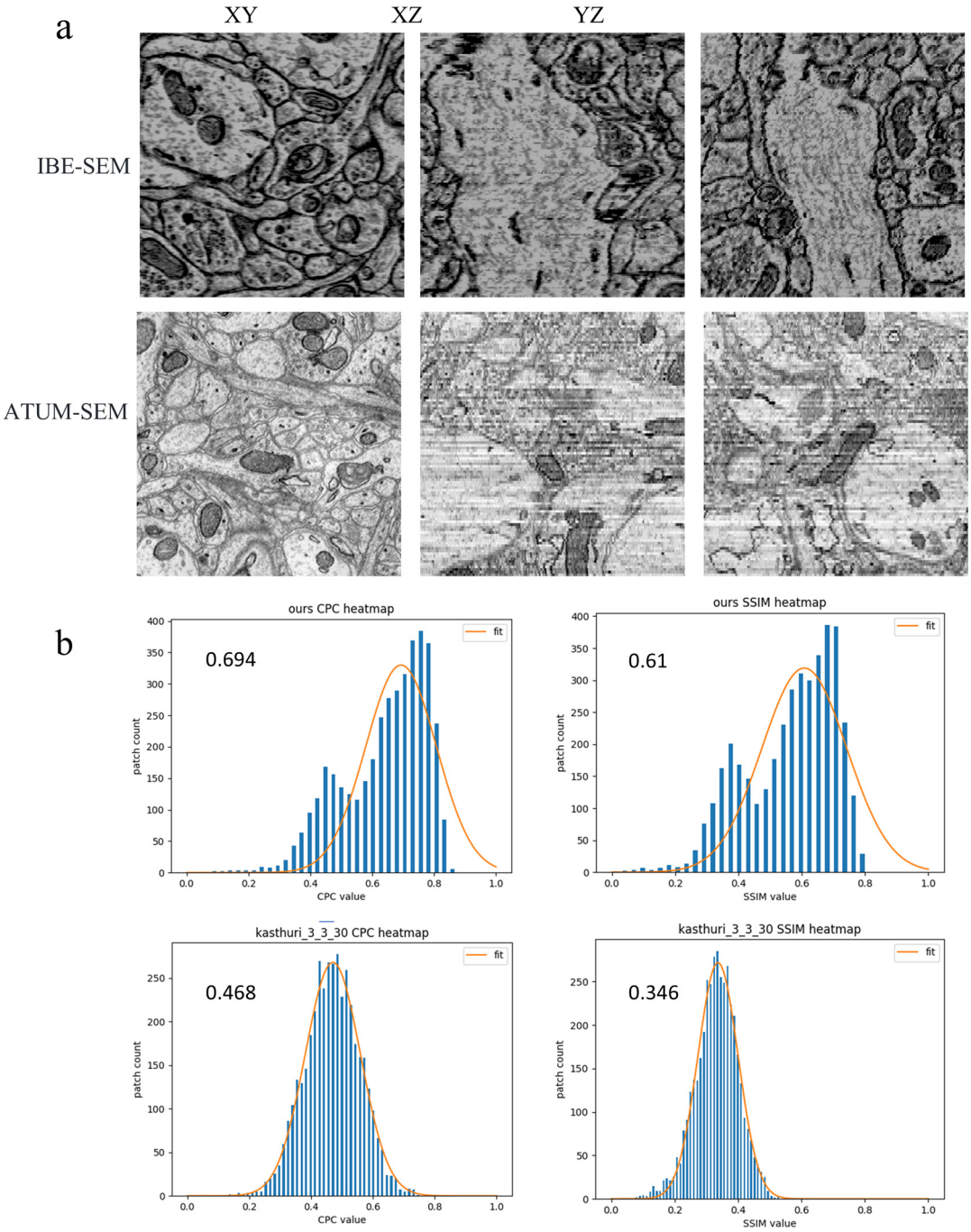

Supplementary Fig. 5. The comparison between volumes of different imaging pipeline. Three rows correspond IBE-SEM volume (4×4×20nm) and ATUM-SEM volume (Kasthuri, 3 nm × 3 nm × 30 nm), respectively. **a.** Qualitative comparison: xy, xz and yz views. Compared to ATUM-SEM volumes, the neuronal membrane structures in our IBE-SEM volumes exhibit higher contrast and are more easily identifiable across all three views. In x-z and y-z views, synaptic vesicles are distinguishable in our volumes, however blurred in other volumes. Scale bar: 1μm. **b.** Quantitative comparison: histograms of CPC and SSIM indicators. The brown line represents the Gaussian distribution fitting curve of the histogram. The numerical value represents the peak coordinate of the Gaussian distribution.

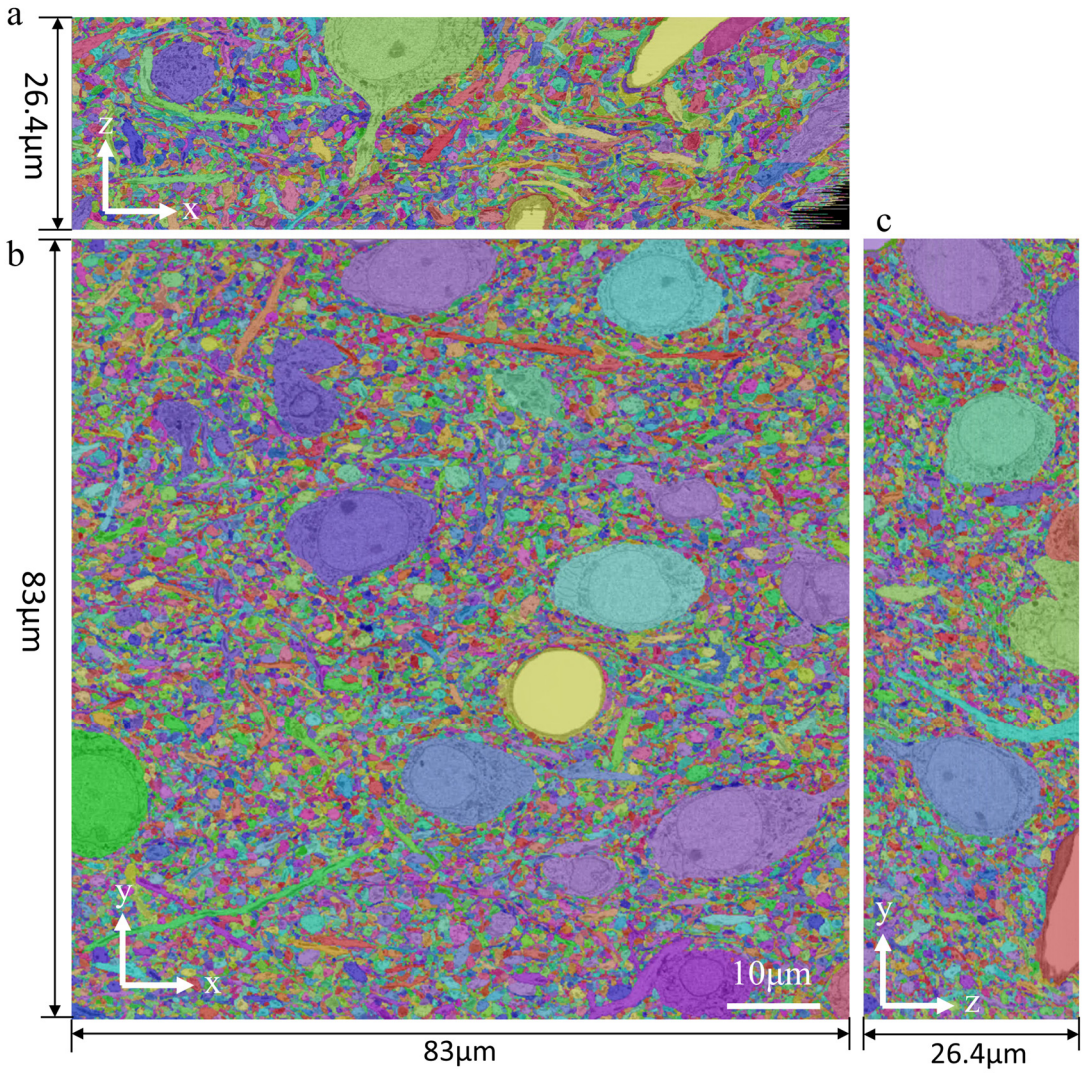

Supplementary Fig. 6. The x-y, x-z, and y-z views of 83um × 83um × 102um volume reconstruction result.

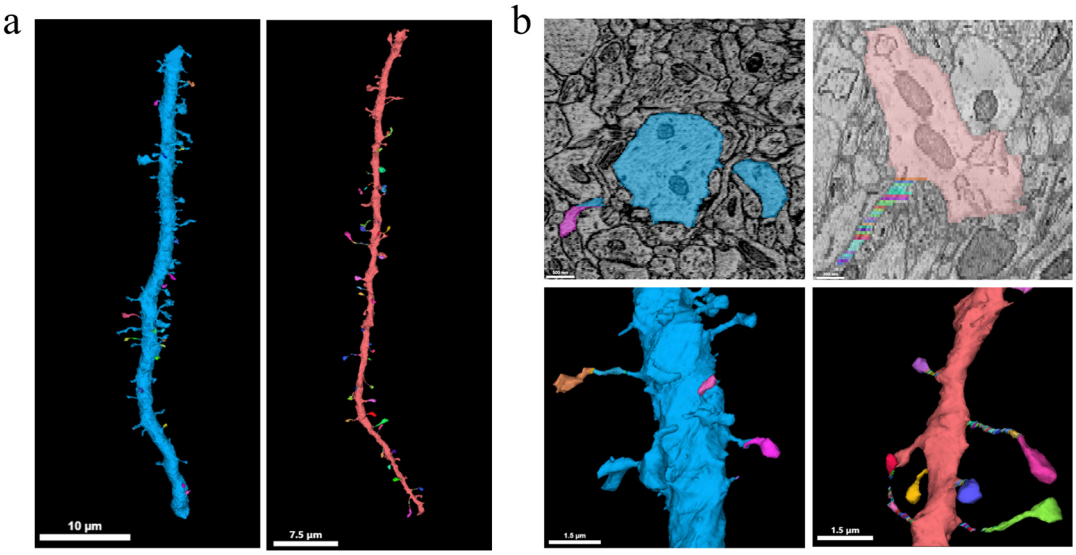

Supplementary Fig. 7. Dendrites reconstructions comparison with ATUM-SEM. a. Proofread dendrites with broken segments from IBE-SEM volume (blue) and ATUM-SEM volume (pink). **b.** Examples of broken spine necks and heads, roughly extending along the cutting direction.

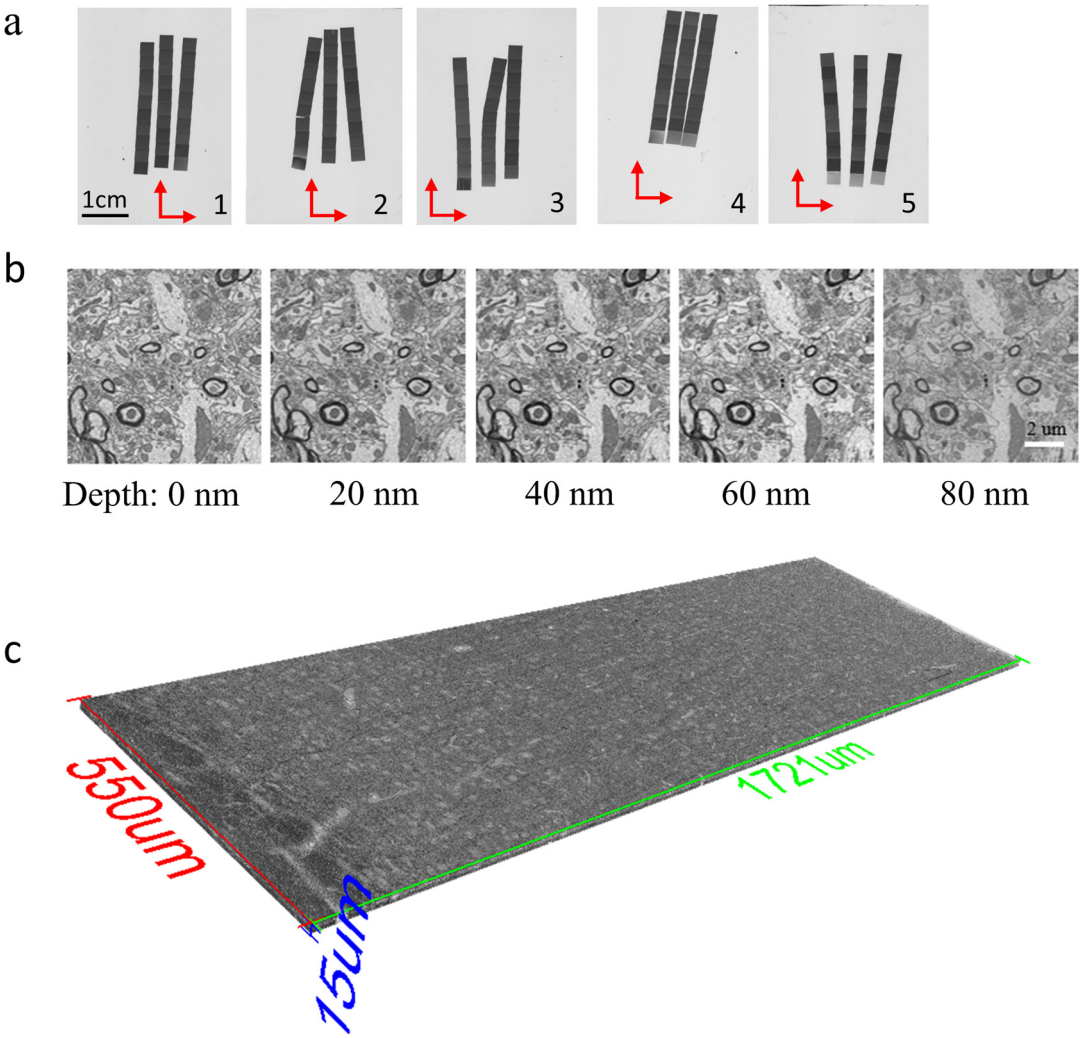

Supplementary Fig. 8. Imaging of a whole mouse cortex by the continuous section etching thinning imaging. a. A total of 150 sections, each 100 nm thick, were obtained and collected on five silicon pieces. **b**. Selected raw images, one every 20nm of etching thinning depth, are shown, spanning a single thick section. Scale Bar, 2um. **c.** A stitched stack is shown as a 3D volume, which size is 1721um * 550um * 15um.

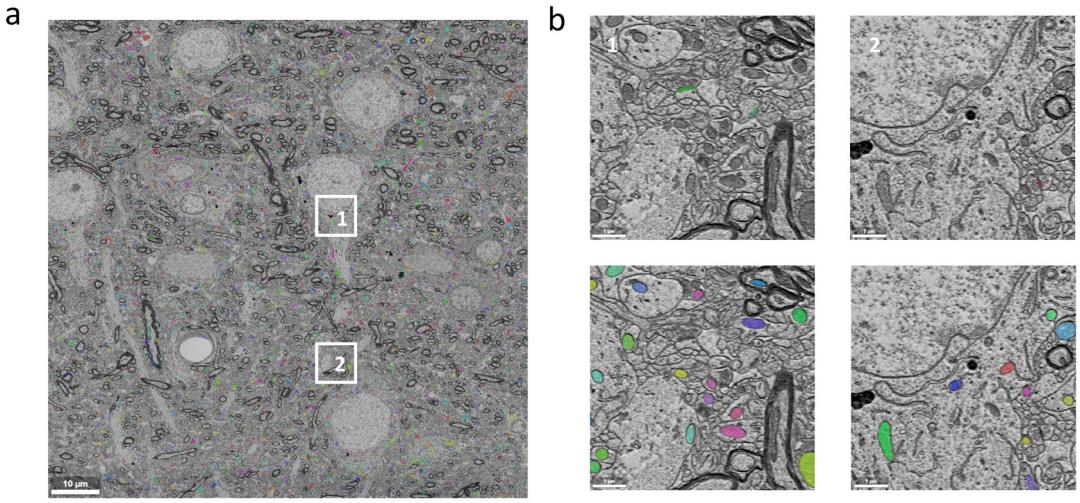

Supplementary Fig. 9 | Reconstruction of ultrastructures for millimeter scale IBE-SEM volume. a. Reconstructed synapses and mitochondria. **b.** Two cutouts from (A) with reconstructed synapses and mitochondria, respectively.

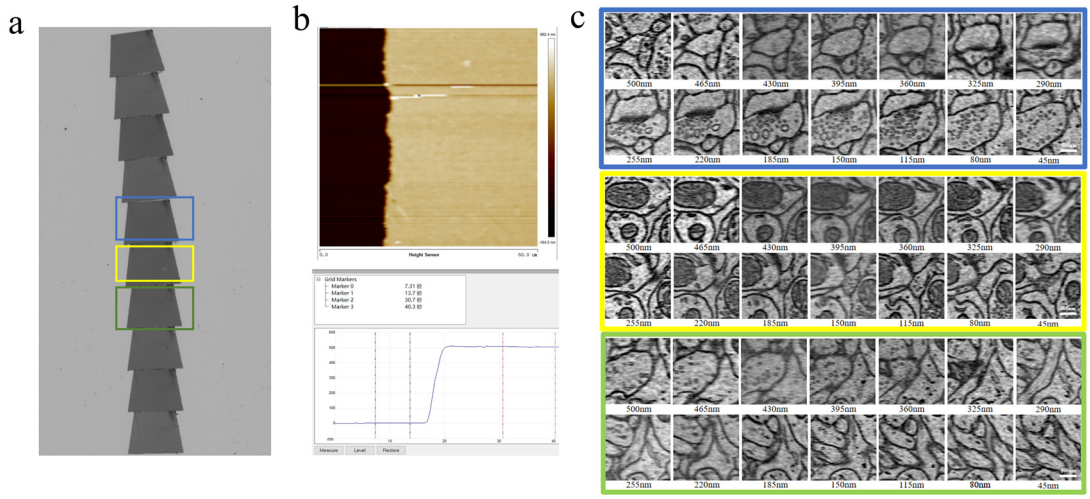

Supplemental Fig. 10 | IBE-SEM imaging in 500 nm-thickness sections. a. The overview of the sections. **b.** The atomic force microscope is applied to test the real thickness of the sections. **c.** Example images from 13 IBE-SEM runs performed on the sections of the mouse brain. Scale bar, 500 nm.

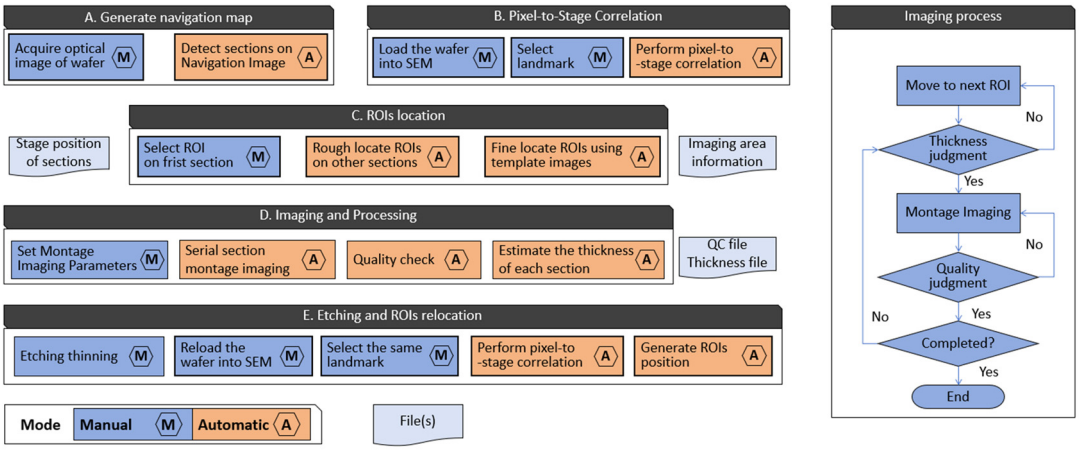

Supplementary Fig. 11. The entire imaging process of the continuous section etching thinning imaging pipeline. A. ROI localization imaging process. (a) Firstly, use an optical camera to capture an overview image of the wafer, and then use section annotation software to detect and mark the contours of the sections on the wafer overview image. (b) Load the wafer into the electron microscope and use positioning software to achieve coordinate correlation between the wafer overview image and the sample stage. (c) Select and semi-automatically locate the ROI of each section in the positioning software. (d) By setting the section ROI positioning file and imaging parameters, the imaging software runs semi-automatically and checks the image quality in real time. (e) Etching thinning and re ROI positioning, the new ROI positioning file will be reused in step (d). B. Detailed imaging process for A-(d).

References

[1] T. A. Jarrell *et al.*, "The connectome of a decision-making neural network," *science,* vol. 337, no. 6093, pp. 437-444, 2012.

[2] M. Zhen and A. D. Samuel, "C. elegans locomotion: small circuits, complex functions," *Current opinion in neurobiology,* vol. 33, pp. 117-126, 2015.

[3] T. Ohyama *et al.*, "A multilevel multimodal circuit enhances action selection in Drosophila," *Nature,* vol. 520, no. 7549, pp. 633-639, 2015.

[4] J. Ngai, "BRAIN 2.0: Transforming neuroscience," *Cell,* vol. 185, no. 1, pp. 4-8, 2022.

[5] D. Witvliet *et al.*, "Connectomes across development reveal principles of brain maturation," *Nature,* vol. 596, no. 7871, pp. 257-261, 2021.

[6] Z. Zheng *et al.*, "A complete electron microscopy volume of the brain of adult Drosophila melanogaster," *Cell,* vol. 174, no. 3, pp. 730-743. e22, 2018.

[7] M. Winding *et al.*, "The connectome of an insect brain," *Science,* vol. 379, no. 6636, p. eadd9330, 2023, doi: 10.1101/2022.11.28.516756.

[8] A. Motta *et al.*, "Dense connectomic reconstruction in layer 4 of the somatosensory cortex," *Science,* vol. 366, no. 6469, p. eaay3134, 2019.

[9] J. Kornfeld and W. Denk, "Progress and remaining challenges in high-throughput volume electron microscopy," *Current opinion in neurobiology,* vol. 50, pp. 261-267, 2018.

[10] J. S. Phelps *et al.*, "Reconstruction of motor control circuits in adult Drosophila using automated transmission electron microscopy," *Cell,* vol. 184, no. 3, pp. 759-774. e18, 2021.

[11] C. S. Xu, S. Pang, K. J. Hayworth, and H. F. Hess, "Enabling FIB-SEM systems for large volume connectomics and cell biology," *bioRxiv,* p. 852863, 2019.

[12] K. J. Hayworth *et al.*, "Gas cluster ion beam SEM for imaging of large tissue samples with 10 nm isotropic resolution," *Nature methods,* vol. 17, no. 1, pp. 68-71, Jan. 2020, doi: 10.1038/s41592-019-0641-2

[13] J. Harper, J. Cuomo, P. A. Leary, G. Summa, H. Kaufman, and F. Bresnock, "Low energy ion beam etching," *Journal of the Electrochemical Society,* vol. 128, no. 5, p. 1077, 1981.

[14] N. Kasthuri *et al.*, "Saturated reconstruction of a volume of neocortex," *Cell,* vol. 162, no. 3, pp. 648-661, 2015.

[15] S. Popovych *et al.*, "Petascale pipeline for precise alignment of images from serial section electron microscopy," *Nature communications,* vol. 15, no. 1, p. 289, 2024.

[16] Z. Wang, A. C. Bovik, H. R. Sheikh, and E. P. Simoncelli, "Image quality assessment: from error visibility to structural similarity," *IEEE transactions on image processing,* vol. 13, no. 4, pp. 600-612, 2004.

[17] M. Björkman, N. Bergström, and D. Kragic, "Detecting, segmenting and tracking unknown objects using multi-label MRF inference," *Computer Vision and Image Understanding,* vol. 118, pp. 111-127, 2014.

[18] M. FISCHLER AND, "Random sample consensus: a paradigm for model fitting with applications to image analysis and automated cartography," *Commun. ACM,* vol. 24, no. 6, pp. 381-395, 1981.

[19] T. Xin *et al.*, "A novel registration method for long-serial section images of EM with a serial split technique based on unsupervised optical flow network," *Bioinformatics,* vol. 39, no. 8, p. btad436, 2023.

[20] Y. Jiang *et al.*, "Synaptic degeneration in the prefrontal cortex of a rat AD model revealed by

volume electron microscopy," *Journal of Molecular Cell Biology,* vol. 14, no. 3, p. mjac012, 2022.

[21] J. Liu *et al.*, "Fear memory-associated synaptic and mitochondrial changes revealed by deep learning-based processing of electron microscopy data," *Cell reports,* vol. 40, no. 5, 2022.

[22] F. Isensee, P. F. Jaeger, S. A. Kohl, J. Petersen, and K. H. Maier-Hein, "nnU-Net: a self-configuring method for deep learning-based biomedical image segmentation," *Nature methods,* vol. 18, no. 2, pp. 203-211, 2021.

[23] P. Zhou, J. Feng, C. Ma, C. Xiong, and S. C. H. Hoi, "Towards theoretically understanding why sgd generalizes better than adam in deep learning," *Advances in Neural Information Processing Systems,* vol. 33, pp. 21285-21296, 2020.

[24] L.-C. Chen, G. Papandreou, I. Kokkinos, K. Murphy, and A. L. Yuille, "Deeplab: Semantic image segmentation with deep convolutional nets, atrous convolution, and fully connected crfs," *IEEE transactions on pattern analysis and machine intelligence,* vol. 40, no. 4, pp. 834-848, 2017.